Materials & Design 209 (2021) 109985

Contents lists available at ScienceDirect

Materials & Design

journal homepage: www.elsevier.com/locate/matdes

Multiscale investigation of the influence of geometrical imperfections, porosity, and size-dependent features on mechanical behavior of additively manufactured Ti-6Al-4V lattice struts

Atikom Sombatmai [a], Vitoon Uthaisangsuk [a], Somchai Wongwises [b,c], Patcharapit Promoppatum [a,*]

[a] Center for Lightweight Materials, Design, and Manufacturing, Department of Mechanical Engineering, Faculty of Engineering, King Mongkut's University of Technology, Thonburi, Bangkok 10140, Thailand
[b] Department of Mechanical Engineering, Faculty of Engineering, King Mongkut's University of Technology Thonburi (KMUTT), Bangmod, Bangkok 10140, Thailand
[c] National Science and Technology Development Agency (NSTDA), Pathum Thani 12120, Thailand

HIGHLIGHTS

- The effects of manufacturing defects on mechanical behavior of lattice struts were investigated.
- Struts of different sizes and orientations were additively made and subjected to tensile test.
- Micro-computed tomography was used to quantify both internal and external defects.
- The impact of different defects was assessed using the FE model.

GRAPHICAL ABSTRACT

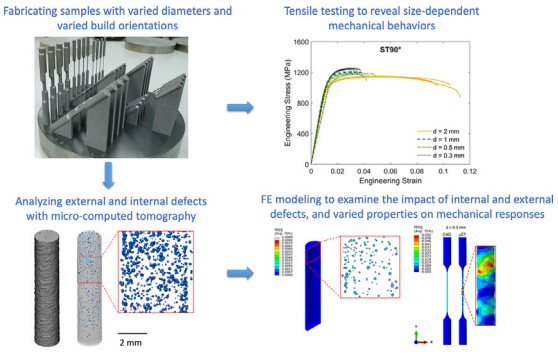

ARTICLE INFO

Article history:
Received 17 May 2021
Revised 7 July 2021
Accepted 11 July 2021
Available online 16 July 2021

Keywords:
Additive manufacturing
Laser powder bed fusion
Micro-computed tomography
Effects of defects
Mechanical properties
Lattice structures

ABSTRACT

Various manufacturing defects are known to have significant impact on the mechanical properties of lattice structures. Therefore, defects-embedded FE models are essential for accurate mechanical prediction. However, previous studies often focused on the investigation of complete lattice structure models. As a result, the comprehensive investigation of defects in a single strut remained elusive. The present study investigated five different defects on a single strut, namely undersizing/oversizing, diameter variation, offset of the cross section, internal voids, and local mechanical properties. It was found that the undersizing and oversizing were the primary factor affecting the discrepancy between experiments and numerical predictions for most cases. The diameter variation and offset of the cross section were seen to be dominant for small struts, especially those with 45° build orientation. Furthermore, even though the onset of localization could be observed due to the presence of voids, they had a negligible impact on elastic and initial yielding responses, partly because of their low volume fraction. Besides, the effect from geometrical inaccuracies and varied properties were mostly comparable although that of the former was more dominant in smaller samples. In addition, the sensitivity from the μCT voxel size affected both global behaviors and localization.

* Corresponding author.
E-mail address: patcharapit.pro@kmutt.ac.th (P. Promoppatum).

https://doi.org/10.1016/j.matdes.2021.109985
0264-1275/

1. Introduction

Additive manufacturing is widely adopted due to its ability to produce intricate components which cannot be fabricated with traditional processes [1]. Laser powder bed fusion (L-PBF) is among the most commonly used technique owing to its ability to produce complex parts with high precisions [2]. The L-PBF process enables the fabrication of lattice structures which hold advantages thanks to their exceptional strength-to-weight ratio [3,4] and high energy absorption [5,6]. Because of these reasons, aerospace [7], automotive [8], and medical [9] industries adopted these structures in various applications. Nonetheless, despite the advantages of the L-PBF lattice structures, manufacturing defects are among the main concerns affecting mechanical integrities [10,11]. Geometrical imperfections often originate from manufacturing defects, caused by sub-optimal process conditions leading to incomplete or overmelting of metal powders [12]. Furthermore, even though process parameters could be optimized [13,14], the geometry of the L-PBF part may still be affected by build orientations [15]. Thus, without the post-surface finishing, geometrical imperfections are mostly inevitable in the L-PBF components. The lack of proper consideration of defects in the Finite Element (FE) models of L-PBF lattice structures would lead to a significant difference between experiments and numerical simulation, resulting in difficulty during the designing process [10,11]. Consequently, various studies have attempted to include local geometrical imperfections in FE models for a more accurate mechanical prediction.

Computed Tomography (CT) and Micro-Computed Tomography (μCT) are non-destructive testing techniques, producing series of two-dimensional images along the cross sections [16]. Based on two-dimensional images, the characterizations of internal and external defects such as internal voids, dimensions, and shapes could be achieved. In addition, two-dimensional images can be reconstructed into three-dimensional models. The reconstructed FE models have been created and used by various researchers to explore the influence of geometrical imperfections of additively manufactured lattice structures. Leary et al. [17,18] created FE models embedded with geometrical imperfections from μCT images to investigate the deformation and failure mechanisms under compression of AlSi12Mg and Inconel 625 lattice structures. Results showed that the reconstructed FE models captured experimental results relatively well, and they were able to illustrate the stress concentration resulting from the geometrical imperfections. Boniotti et al. [19] examined the strain localization of the L-PBF lattice structures using the Digital Image Correlation (DIC) technique. They compared the strain concentration factor (K_ε) from the experiments with that of as-designed and reconstructed FE models. As expected, K_ε from reconstructed FE models were closer to experimental results than that from the ideal models. The difference between measured and simulated K_ε reduced from 31 % to 9 % when the reconstructed FE model was used instead of the ideal one. A subsequent study was reported by Geng et al. [20] who also emphasized the critical role of surface defects on the reduction of strength and failure resistance of additively manufactured lattice structures. These results accentuated the importance of geometrical imperfections in dictating the mechanical behaviors of L-PBF lattice structures.

In addition to the direct reconstruction from the μCT, several studies proceeded with an alternative route by classifying and analyzing geometrical imperfections in forms of statistical distribution. Subsequently, the FE model could be reconstructed from various defect distributions. Ravari et al. [21] defined the diameter variation as the primary surface defect and recreated the FE model based on the inclusion of varied diameters within struts. They concluded that the reconstructed model could improve the accuracy of the predicted elastic modulus and collapse stress. Nonetheless, at least ten intervals for reconstructed struts were suggested to achieve reasonably accurate predictions. Likewise, Lei et al. [22] carried out a similar study for AlSi10Mg lattice structures where the strut diameter variation was taken into account. They also noted the dependency of the strut variation on build angles. Besides, not only was the variation of the strut diameter recognized as the geometrical defect, but the offset of the cross section could also significantly affect mechanical responses. Both Ravari et al. [23] and Dallago et al. [24] developed the reconstructed FE model including the imperfections from the distributed diameter variations and offset of the cross section. Lozanovski et al. [25] studied the variation of the centroid deviation, principal moments of inertia, and principal axis orientations of lattice struts from CT images. Subsequently, the representative FE models including defects in struts were generated, where the predictions of elastic modulus and yield's strength exhibited better agreement with experimental results when compared with those from defect-free FE models.

According to the above studies, the influence of geometrical imperfections on mechanical responses was fully recognized and should be considered in the FE models. Geometrical imperfections could vary based on strut diameters and build orientations. Therefore, many recent studies focused on characterizing defects and mechanical behaviors of individual struts. Zhang et al. assessed diameter variations of lattice struts with various sizes and build orientations [26]. While geometrical features were thoroughly discussed, the impact of defects on mechanical responses was not evaluated. On the other hand, Pegues et al. [27] emphasized the effect of surface roughness on fatigue strength. Small samples and samples with diagonal builds tended to have higher surface roughness, leading to lower fatigue resistance. Furthermore, various size-dependent properties were reported by several studies such as Barba et al. [28], Phutela et al. [29], and Dong et al. [30] among others. Similar observations were reported, in which resultant microstructures and mechanical properties varied strongly with the sample size. Nonetheless, a connection between external defects and microstructures on the mechanical responses was not explicitly discussed in those studies. Moreover, based on the recent review by Benedetti et al. [31], the mechanical responses are influenced not only by defects and microstructures but also residual stress. Both compressive and tensile stresses may form at various locations of samples, and the formation of residual stress may vary with the sample size, build orientations, and process conditions [32-34]. Therefore, the mechanical behaviors in lattice structures were dictated by the competitive relationship among surface defects, microstructures, and residual stress. Although the comprehensive study of these effects on mechanical responses is essential, it is hardly adequate.

Thereby, the present study aims to examine the influence of manufacturing defects such as geometrical imperfections, internal voids, and size-dependent properties on the mechanical responses of L-PBF Ti-6Al-4V lattice struts. Struts were made with different diameters and build orientations. The μCT was used to extract both external and internal defects. Subsequently, the statistical characterization was performed to reveal the dependency of defects on feature sizes and build orientations. Subsequently, various numerical simulations including as-designed, μCT reconstructed, and representative FE models were evaluated and compared. Tensile specimens were fabricated, and testing results were used to correlate the size-dependent elastic and initial yielding behaviors and to assess the accuracy of different FE models. Ultimately, we seek to shed light on understanding various factors which could affect single strut mechanical properties. As a result, this knowledge could contribute to the reconstruction of L-PBF lattice structure models

which could be performed with satisfactory accuracy under acceptable computational resources.

2. Experimental methods

Single struts (SS) and tensile specimens (ST) with varied diameters and build orientations were made to investigate internal and external defects, and mechanical responses. Detailed descriptions of a manufacturing process, sample's dimension, and experimental investigation were discussed as follows.

2.1. Sample fabrications

All samples were fabricated using TRUMPF TruPrint 1000 under default process parameters and print strategies for Ti-6Al-4V. Samples were made under low oxygen content, and no heat treatment was performed after the build was completed. Table 1 displays the processing parameters used in the present work, where two different settings were used for in-skin and border patterns. Fig. 1 shows the scan strategies consisting of in-skin and border patterns for samples with diameters of 0.3 and 2 mm and two build orientations. For a sample with a diameter of 2 mm, two borderlines were observed, and a uniform scan pattern was used for the interior region. On the other hand, only a single borderline and no in-skin pattern was used for samples with 0.3 mm diameter.

In addition, seven single struts (SS) with diameters of 0.3, 0.4, 0.5, 0.75, 1, 1.5, and 2 mm were created with two build angles of 45° and 90° as shown in Fig. 2a. According to Fig. 2a, struts were built on a solid support such that they could be easily removed using the wire electrical discharge machining (wire-EDM). These sample sizes and build angles were chosen as they were normally found in various lattice structures. SS samples were designed to assist the examination of internal and external defects. Therefore, they were built without handles and relatively small size. On the other hand, the tensile samples (ST) shown in Fig. 2b were made for mechanical testing. Consequently, the ST specimens were noticeably larger than SS ones. The ST samples were also made with varying diameters and two build angles. Nonetheless, only four diameters of 0.3, 0.5, 1, and 2 mm were made for the ST samples. Fig. 2b illustrated the dimension of all ST samples, in which the design of the ST samples was modified according to the standard method for tension testing of metallic materials (ASTM E8/E8M) [35].

2.2. Non-destructive evaluations of internal and external defects

The present study classified defects into internal and external types. Internal defects are voids that could be attributed to the lack of fusion, balling effect, keyholing, and the release of gas trapped in powders [13]. The external defects are the geometrical imperfections which are divided into the undersizing/oversizing, diameter variation and the offset of the strut cross sections [11,24,36].

Both internal and external defects were examined using high-resolution μCT, the Bruker SkyScan 1173. The energy and current of the X-ray source were 130 kV and 61 mA, respectively. The μCT would provide series of two-dimensional projected images. The resolution of the μCT was determined by the voxel size. The voxel size of 7 μm was used for the SS samples and 12 μm for the ST samples. The larger voxel size in the latter sample was to maintain reasonable scanning time. In total, seven SS and four ST specimens of different sizes for each build orientation were subjected to the CT scan. Results from every CT scan were used to characterize internal and external defects, and to perform FE simulation. A raw image from the CT scan was shown in Fig. 3.

In addition, images were imported using the ScanIP (Simpleware Ltd., Exeter, UK) to reconstruct into three-dimensional objects [37]. The contrast and noise were corrected with thresholding as seen in Fig. 3. After thresholding, the binary images of solid and voids would be obtained. The fill hole function was optional and used only when the three-dimensional objects without internal voids need to be created. Based on processed images, external defects such as equivalent diameter and the offset of the cross section could be analyzed accordingly. Fig. 4 illustrated two-dimensional images of the SS samples and their reconstruction into three-dimensional objects.

Table 1
Processing parameters for the L-PBF machine TRUMPF TruPrint 1000.

Parameters	In-skin	Border
Spot size	55 μm	55 μm
Laser power	125 W	150 W
Laser speed	905 mm/s	1600 mm/s
Hatch spacing	80 μm	80 μm
Layer thickness	20 μm	20 μm

2.3. Mechanical testing

Tensile testing was performed for all ST samples using the universal testing machine, Tinius Olsen - H50KS with 1 kN load cell for samples with diameters of 0.3, 0.5, and 1 mm and 50 kN load cell for a sample with a diameter of 2 mm. The tensile testing was operated under quasi-static loading conditions with a strain rate of less than 0.001 s^{-1}. Due to the difficulty in collecting displacement for small samples, the Digital Image Correlation (DIC) based technique using a GOM Aramis system (ARAMIS, GOM Co., Germany) was utilized as a virtual extensometer to collect deformation with a resolution of 1 fps. The displacement from the DIC was used for strain calculation. While the force data was collected from the tensile testing machine, it is important to note that the as-designed area was not used for the stress calculation. Since the discrepancy between as-designed and as-built cross-sectional areas was anticipated, the use of as-designed areas to determine the stress magnitude could be misleading. Thus, we relied on the average equivalent area at the gauge length from μCT images for the calculation of stress.

3. Numerical simulation

3.1. Reconstructed Finite Element models from μCT

The FE mesh for SS and ST specimens was created using the ScanFE (Simpleware Ltd., Exeter, UK) based on three-dimensional objects from Section 2.2 [38]. Fig. 5a and Fig. 5b showed the reconstructed FE models with external defects for SS and ST samples, respectively. In addition, Fig. 5c showed the reconstructed model with internal defects. Of note, voids from the μCT could be presented in different sizes and morphologies. Therefore, attempting to account for every actual pore geometry in FE models would make the meshing increasingly arduous. Therefore, we simplified the inclusion of internal defects by using only spherical voids with effective diameters and locations obtained from the μCT. In other words, spherical voids in the domain would have various diameters. Such simplification preserved the total volume fraction of voids while minimizing the computational demand. Also, since our aim was to differentiate between the effects from external and internal defects, only a simplified cylinder was used as a base geometry when studying the effect of internal voids.

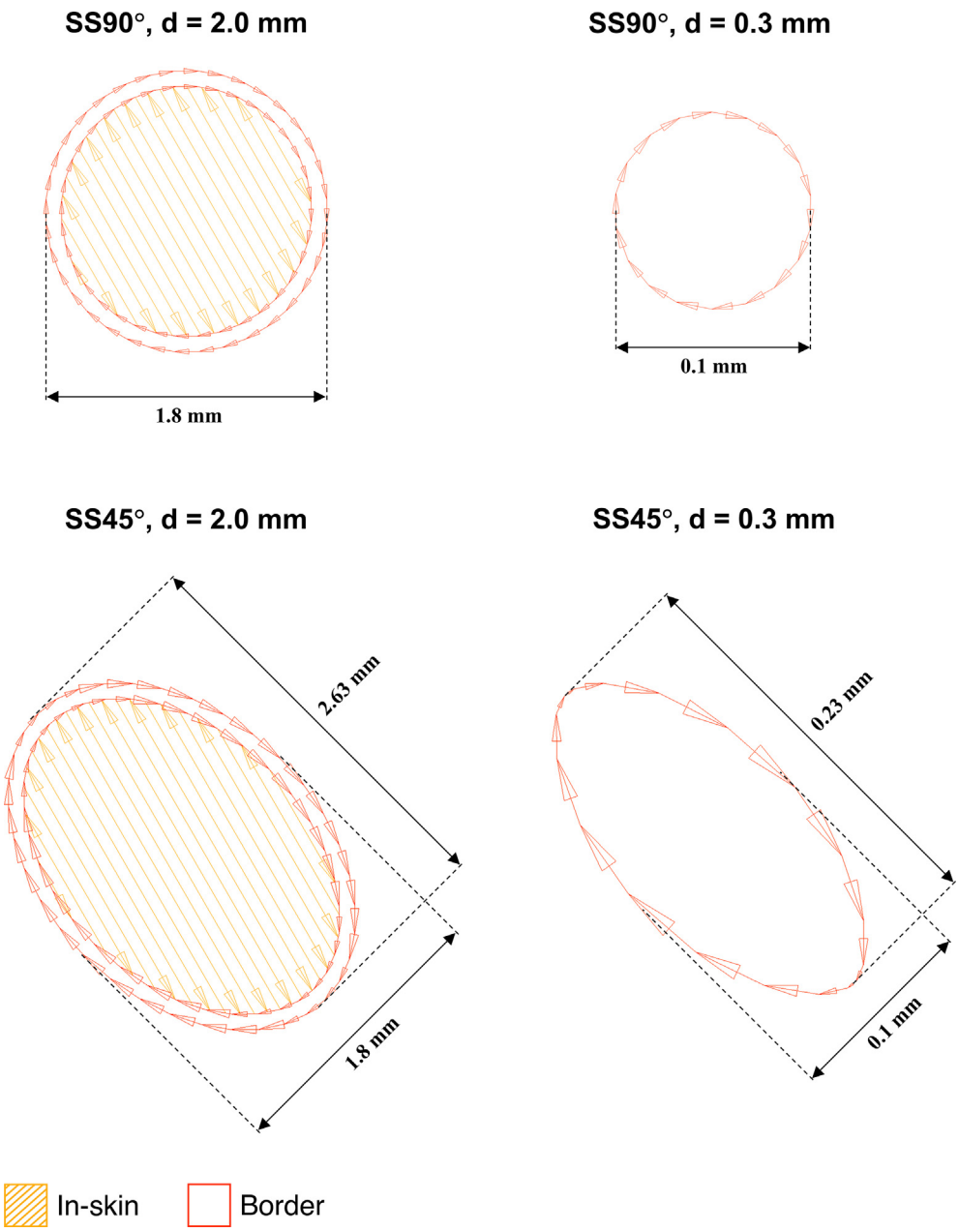

Fig. 1. Scan strategies consisting of in-skin and border patterns for the samples with diameters of 2 and 0.3 mm and with build angles of 90° and 45°.

3.2. Boundary conditions, materials, and meshes for mechanical simulation

A mechanical simulation was performed using the commercial FE software ABAQUS/Implicit. The tensile loading was applied in a quasi-static condition. The displacement boundary conditions were imposed at top and bottom surfaces, and rotations were constrained. For numerical results of the SS specimens shown in Sections 4.2 and 4.3, we adopted the flow stress for the L-PBF of Ti-6Al-4V reported by He et al. [39] for all simulations. On the other hand, only numerical results in Section 4.4 utilized the experimental flow stress, obtained in the present work. The Voce hardening model as shown in Eq. (1) was used to fit with experiments. The fitted constants of σ_{y0}, H, and β, for He et al. results were 1034 MPa, 226 MPa, and 173 respectively. The implementation of the material model was done through a Fortran-based subroutine, UHARD. In addition, Young's Modulus and Poisson's ratio were 100 GPa and 0.3, respectively [29].

Of note, Young's modulus adopted in the present study was lower than that of bulk samples, which was known to be between 110 and 119 GPa [40]. The reason was according to recent experimental reports, in which strut specimens exhibited lower Young's modulus than that of the bulk [28,29,41].

$$\sigma_y = \sigma_{y0} + H(1 - exp(-\beta\varepsilon_p)) \quad (1)$$

In addition, linear tetrahedral elements (C3D4) were used, and the mesh sensitivity analysis was performed for the SS sample with a diameter of 0.3 mm. Numerical results for mesh sensitivity analysis were included in the appendix. According to the sensitivity analysis, the minimum and maximum mesh sizes for the 0.3 mm specimen were between 7.5 and 15 μm. Nonetheless, since specimens with various sizes were used in the present work, the mesh

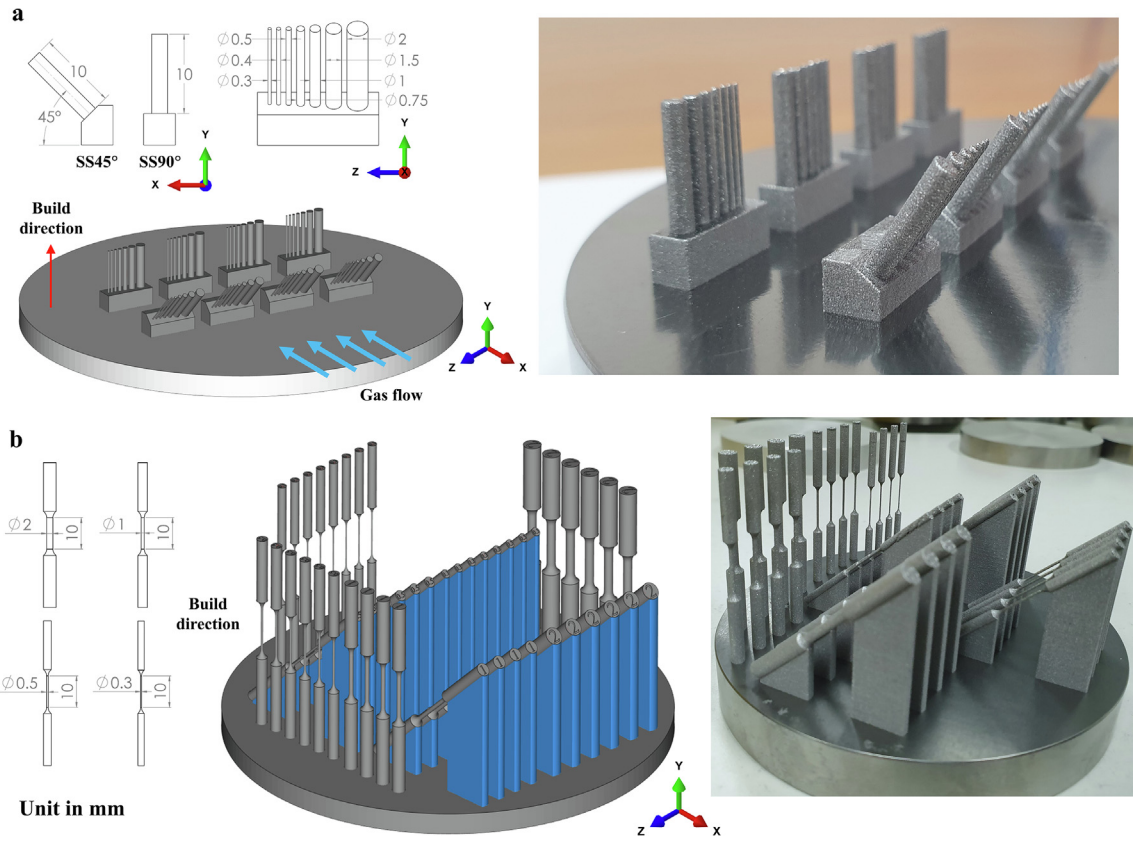

Fig. 2. Dimensions and build platform of a) single struts (SS) and b) tensile specimens (ST).

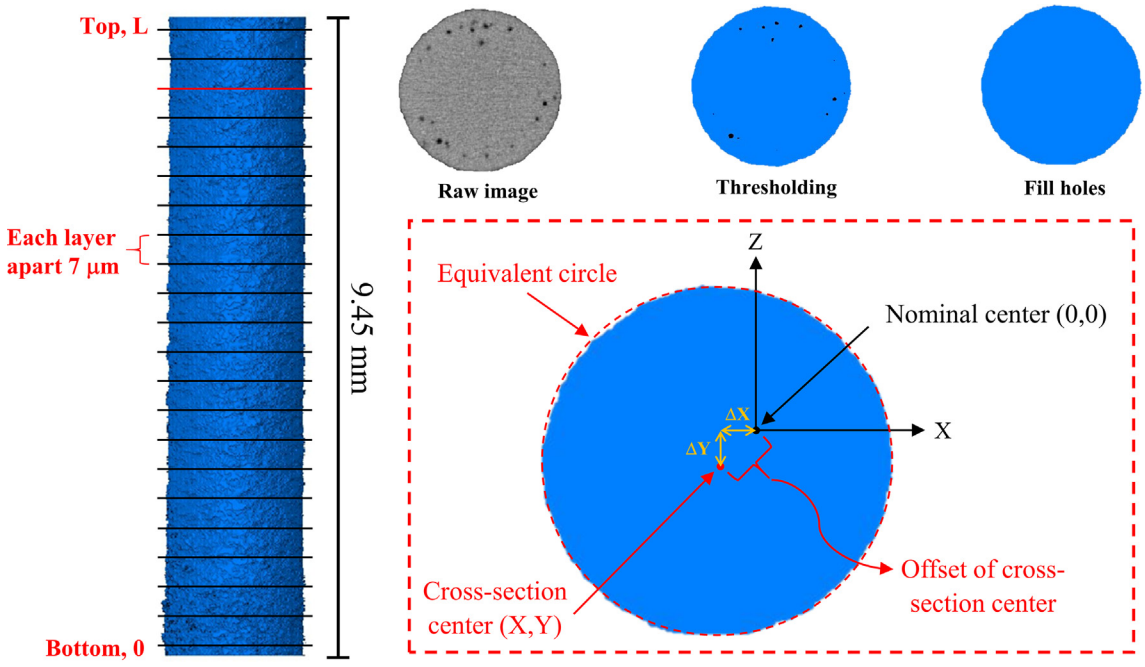

Fig. 3. Extraction of the strut's diameter variation and the offset of the strut's cross section from μCT images.

size of other samples was determined according to the ratio of their diameters. The ratio of mesh size to diameter was between 0.025 and 0.05 as shown in Fig. 5. The total element numbers were approximately 1 million for all samples regardless of their sizes.

4. Results and discussion

Section 4.1 evaluated size- and orientation-dependent external defects on SS samples according to the μCT. Followingly, Section 4.2

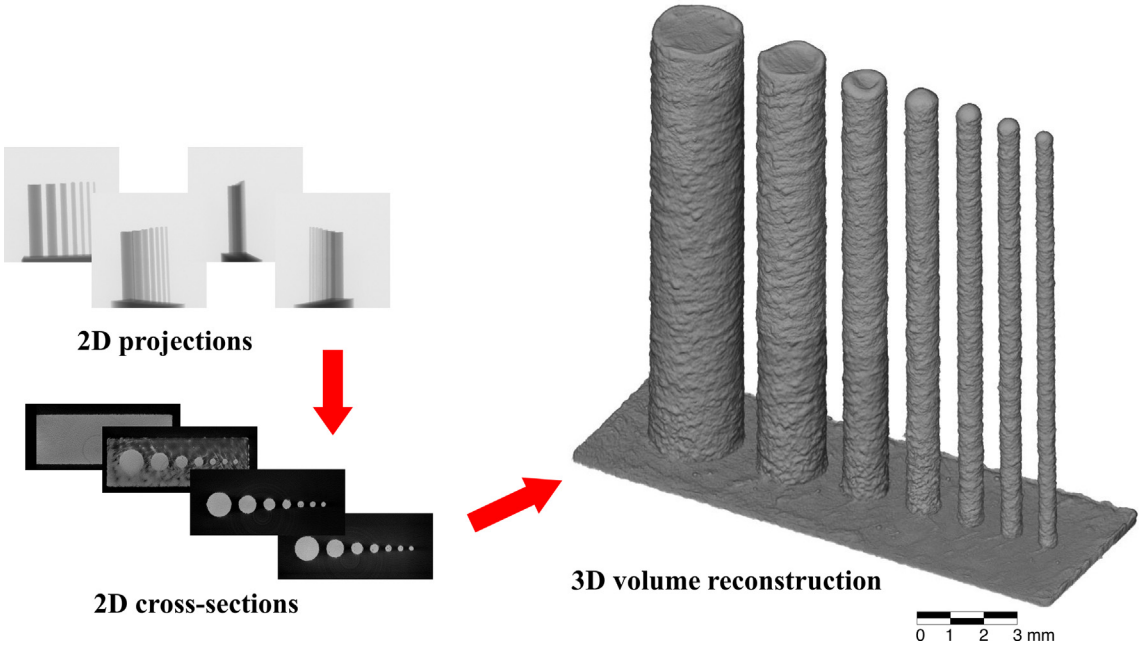

Fig. 4. Reconstruction of three-dimensional objects according to two-dimensional images obtained from the μCT.

assessed numerically the influence of various external defects on mechanical responses. Section 4.3 examined the number of internal defects and evaluated their impact on mechanical prediction. Lastly, Section 4.4 performed mechanical testing on ST samples to reveal size-dependent properties. The discussions of the competition between geometrical errors and varied properties, and the effect of the CT voxel sizes on mechanical prediction were also made.

4.1. Evaluation of external defects

The evaluation of external defects was performed on SS samples with seven different diameters and two build angles. The distribution of the equivalent diameter from μCT images could be found in the appendix. With the voxel size of 7 μm, approximately 1400 images were evaluated in each sample. The mean (μ_d) and standard deviation (s_d) of the equivalent diameter were summarized in Table 2, where experimental strut diameters deviated noticeably from as-designed diameters. In addition, Table 2 illustrated clearly the influence of build angles on the variation of equivalent diameters. The standard deviation of the samples with 45° build angle increased when the sample's size reduced with the range of standard deviation between 7 and 13.3 μm. On the other hand, the standard deviation of the samples with 90° build angle only showed a slight change with samples' size, where the ranges of standard deviation were between 4.7 and 6.6 μm.

Additionally, the mean equivalent diameters were compared with as-designed diameters to indicate the oversizing and undersizing of the SS samples. The difference between experimental and as-designed diameters was reported as the strut diameter error (d_{error}). The negative error referred to the undersizing while the positive error indicated the oversizing. According to d_{error}, most SS samples were undersizing, except those with diameters of 0.3 and 0.4 mm which exhibited the oversizing behaviors. The maximum strut diameter error was around 15%. Determining the cause of the sizing discrepancy would be a challenging task as it would involve several factors such as geometries, process parameters, and scanning strategies which could affect heat transfer mechanisms [42]. Nonetheless, according to Table 2, the general observation was that the struts with 45° build angle were larger than those with 90° build angle. A reason for a larger strut with 45° build angle would be because the down skin surface of struts was placed on top of powders which had much lower thermal conductivity than that of the solid. As a result, poorer heat dissipation for 45° build angle resulted in a larger melt pool size, and thus, a larger strut dimension.

Additionally, Table 3 showed the mean and standard deviation of the offset for all samples. A general observation for the offset was similar to that of the equivalent diameter where the offsets were larger for small struts, especially those with 45° build angle. The information shown in Table 2 and Table 3 could be useful for the reconstruction of defect-embedded FE domains of struts or lattice structures. Nonetheless, it should be noted that the information displayed in both tables was only applicable for process conditions and printing strategies adopted in the present study.

4.2. Influence of external defects on mechanical responses

Even though reconstructed FE domains from the μCT could provide the most realistic evaluation on the effect of external defects, these models were computationally expensive. As a result, finding the representative FE model, which optimizes between the accuracy and required resources, is of interest. Three external defects were considered in the previous section including the diameter variation, the offset of the cross section, as well as the undersizing/oversizing. Among the three defects, the undersizing and oversizing can be considered global defects as they directly alter the overall load-bearing areas. On the other hand, the diameter variation and offset could be seen as the local ones since they primarily induce localization. The localization could be the important factor for the failure mechanism. However, since the present study focuses on the influence of defects on the elastic and initial yielding regimes, the computational model with the mean equivalent diameter from μCT was used as the representative FE model. Therefore, three different FE models were used to study the SS samples, including the reconstructed model from μCT, the model with the mean equivalent diameter from μCT, and as-designed

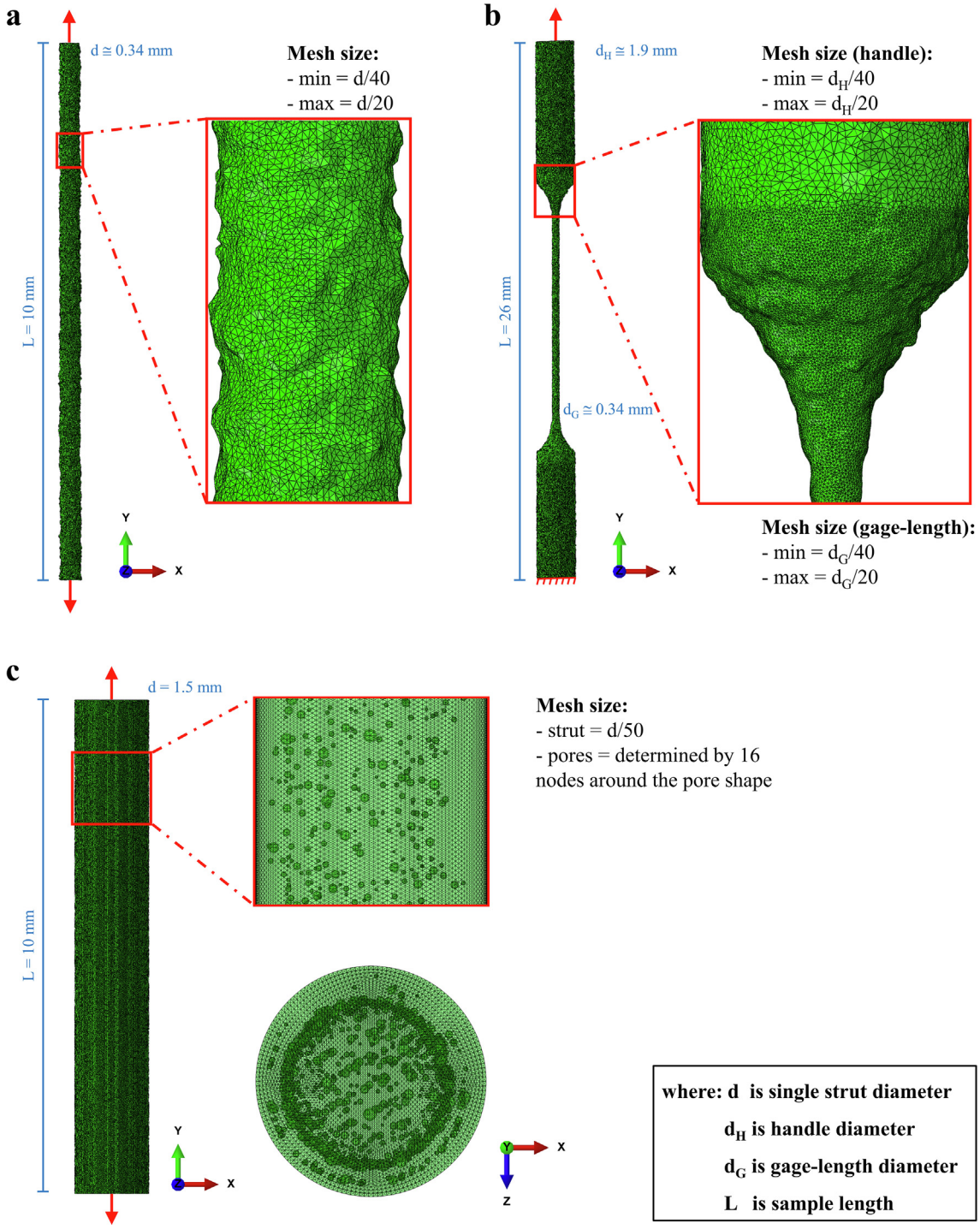

Fig. 5. FE model reconstructed from μCT for the SS and ST samples with the diameter of 0.3 mm and 90° build angle for a) the SS sample with external defects, b) the ST sample with external defects, and c) the SS sample with internal defects.

model, where the abbreviations of μCT, Avg, and CAD were used when discussing these results, respectively.

Fig. 6 showed the prediction of the equivalent plastic strain for the SS samples with diameters of 0.3 and 2 mm and with 90° build angle. Images were extracted at the strut's total strain of approximately 2 %. Three-dimensional equivalent plastic strain fields were displayed for CAD and μCT models. The plastic strain was uniform for the CAD models while the localization was observed for the μCT models. Moreover, the effect of localization seemed to be greater for the strut of 0.3 mm diameter. These results were somewhat expected due to larger diameter variation and offset of the cross section for small struts as shown in Table 2 and Table 3.

Fig. 7a and b show the global mechanical responses by illustrating the Force-Displacement behaviors between different SS specimens. Again, the numerical results from the μCT model were anticipated to provide the most realistic assessment of the mechanical behaviors. There was a general trend observed for all samples, in which the discrepancy in the predicted forces increased with displacement in the elastic regime. Nonetheless, after the yielding, the difference in the predicted forces seemed to be mostly

Table 2
Mean and standard deviation of the equivalent diameters, and the strut diameter error from the μCT images of the SS samples.

d (mm)	90°			45°		
	μ_d (mm)	s_d (mm)	d_{error} (%)	μ_d (mm)	s_d (mm)	d_{error} (%)
0.3	0.34	0.005	11.97	0.35	0.012	16.53
0.4	0.42	0.007	4.74	0.41	0.013	3.15
0.5	0.48	0.006	−4.19	0.50	0.017	−0.14
0.75	0.65	0.005	−13.41	0.68	0.015	−9.04
1	0.89	0.005	−10.45	0.92	0.011	−8.30
1.5	1.37	0.005	−9.02	1.39	0.007	−7.02
2	1.86	0.006	−6.78	1.88	0.007	−5.89

Table 3
Characterization of the offset of the cross section from the μCT images of the SS samples.

d (mm)	SS90°		SS45°	
	μ_{offset} (μm)	σ_{offset} (μm)	μ_{offset} (μm)	σ_{offset} (μm)
0.3	6.67	3.40	9.39	5.49
0.4	6.78	3.62	11.09	6.88
0.5	5.79	2.76	8.04	5.47
0.75	6.32	3.28	9.08	5.33
1	5.26	2.71	7.81	3.99
1.5	5.55	2.62	8.46	4.49
2	4.06	2.06	7.90	4.41

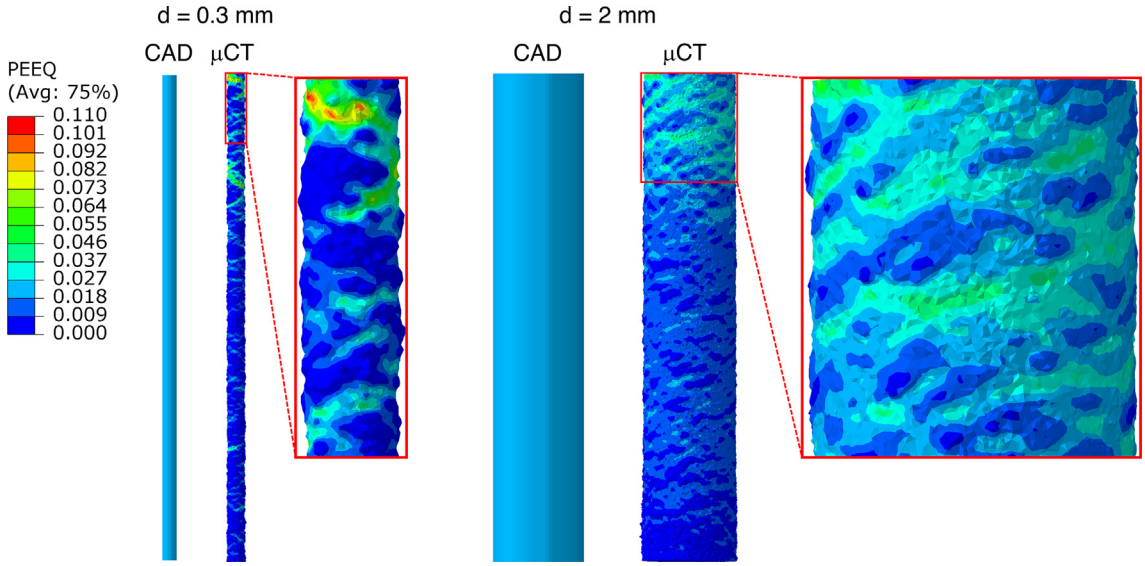

Fig. 6. Simulated equivalent plastic strain, abbreviated by PEEQ, for the CAD and μCT models of the SS samples with diameters of 0.3 and 2 mm and with 90° build angle.

saturated. Therefore, for consistency, the following discussion evaluated the difference in the predicted forces at the displacement of 0.1 mm for all samples.

Fig. 8 illustrated the strut diameter error (d_{error}) together with two reaction force comparison between μCT and CAD models, as well as μCT and Avg models. According to the numerical comparison between μCT and CAD models with 90° build angle, the difference in the predicted forces for struts with diameters of 0.3, 0.5, 1, and 2 mm were 26.5, 2.9, 20.5, and 13.5%, respectively. The difference in the force between μCT and CAD models correlated well with d_{error} as seen from Fig. 8, of which signified the importance of oversizing and undersizing defects. For example, the strut with the diameter of 0.5 mm and 90° angle, which had the lowest d_{error}, also exhibited the smallest difference in the predicted forces between μCT and CAD models. Additionally, the discrepancy of the predicted force between μCT and Avg models reduced to 5.2, 4.6, 3.6, and 0.8 % for struts with diameters of 0.3, 0.5, 1, and 2 mm, respectively. The difference between μCT and Avg models implied the local effects from the diameter variation and the offset, which grew more strongly when the diameter decreased. On the other hand, for specimens with 45° build angle, a similar trend was seen where the maximum difference in the predicted force between μCT and CAD models was about 26 %. Nonetheless, even though the predicted force improved with the use of the Avg models, it was critical to point out that the maximum difference of the reaction force between μCT and Avg models was still around 15 % as seen in struts with diameters of 0.3 and 0.5 mm, respectively. This observation emphasized the more significant roles of the diameter variation and the offset of the cross section for struts with 45° build angle. Hence, according to the comparison in Fig. 8, it was recognized that if the local defects were not dominant, the representative FE model using the mean equivalent diameter could capture the mechanical responses with reasonable accuracy. We see such cases for the struts with large diameters and the build angle

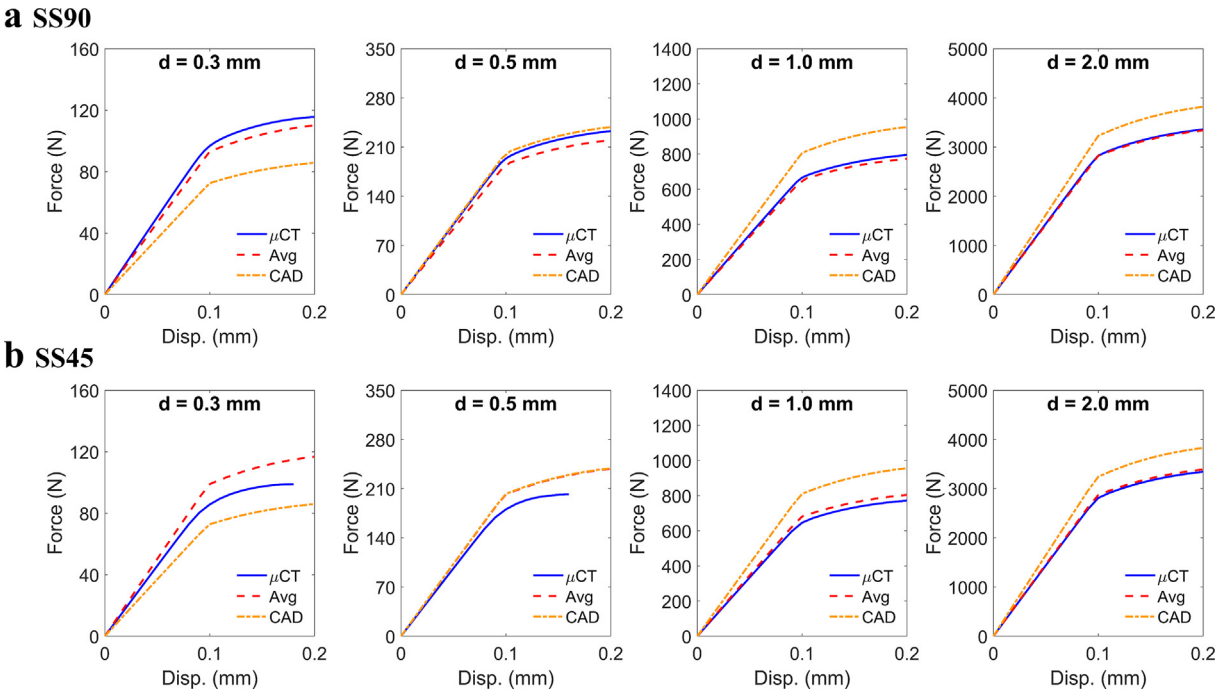

Fig. 7. Numerical prediction of mechanical responses compared between μCT, Avg, and CAD models for SS samples with a) 90° build angle and b) 45° build angle.

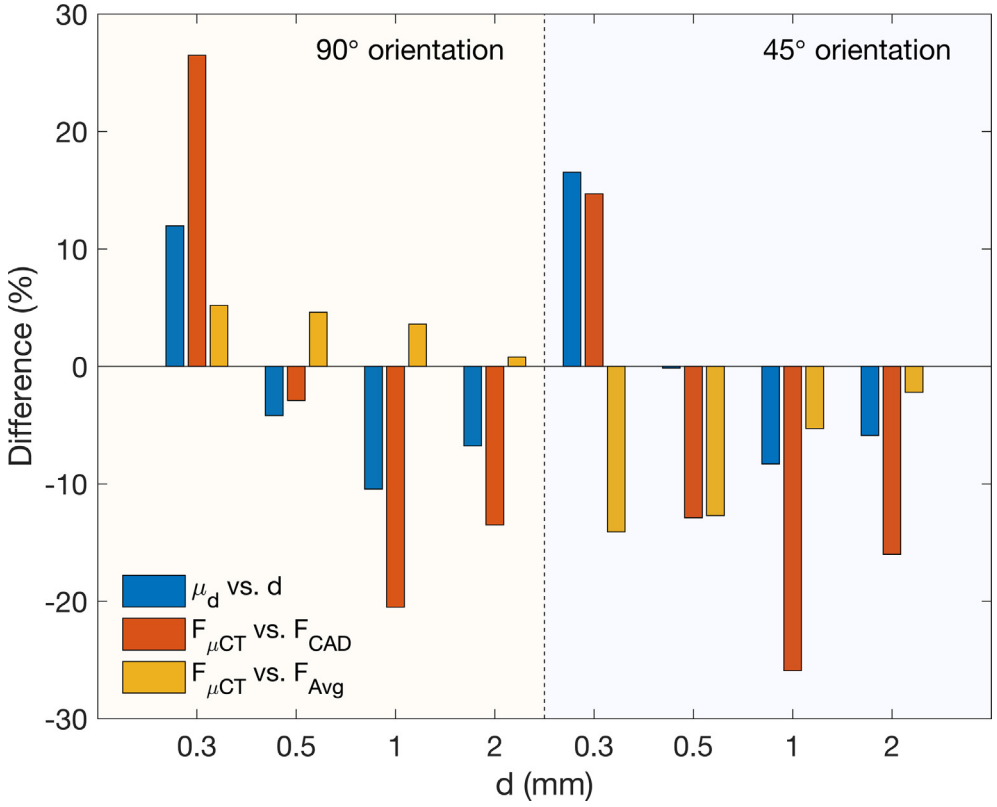

Fig. 8. i) Comparison between mean diameter (μ_d) and as-designed diameter (d), ii) Reaction force comparison between μCT and CAD models, and iii) Reaction force comparison between μCT and CAD models. Reaction forces were collected at the displacement of 0.1 mm.

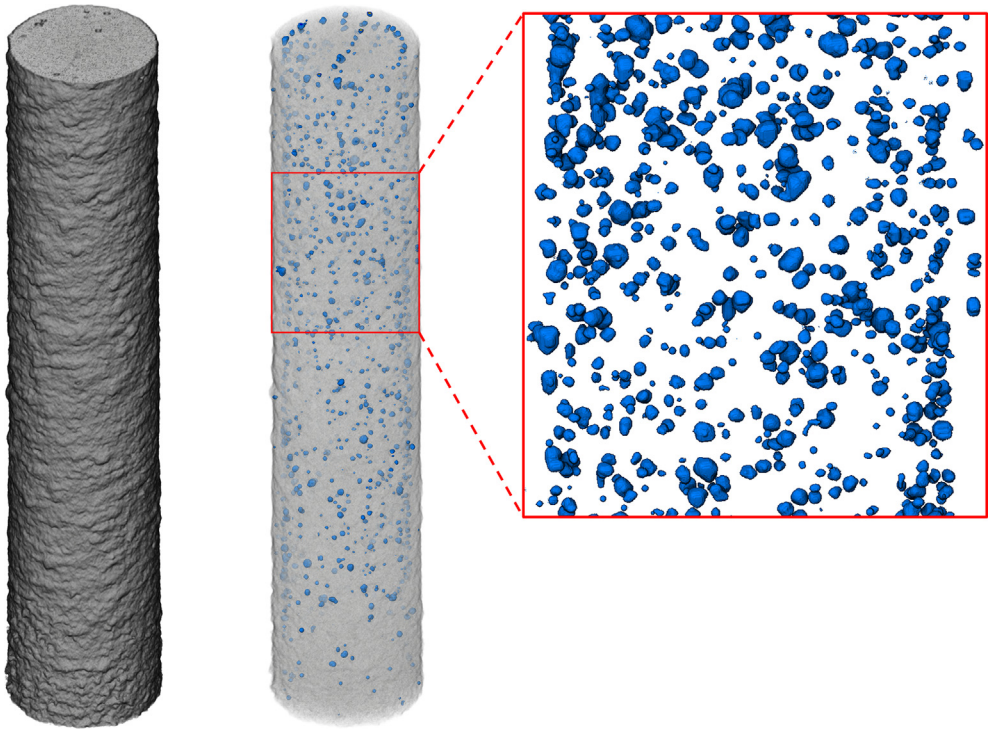

Fig. 9. Internal voids of the SS sample with 2 mm diameter and 90° build angle.

Table 4
Characterization of internal voids on SS samples from the reconstructed μCT models.

d (mm)	Build angle	μ_{void} (μm)	s_{void} (μm)	Total numbers of voids	Void volume fraction
0.3	90	22.3	11.1	44	0.05
0.5	90	34.7	17.8	364	0.85
1	90	33.3	16.8	1116	0.65
2	90	30.4	15.7	2288	0.24
0.3	45	26.4	14.3	44	0.09
0.5	45	30.6	17.8	244	0.44
1	45	29.0	17.7	511	0.24
2	45	26.5	14.7	1036	0.08

of 90°. On the contrary, the incorporation of the local effects may be essential for the mechanical simulation of small struts, especially ones with 45° build angle.

4.3. Evaluation of internal defects and their impact of mechanical responses

Fig. 9 illustrated the distribution of internal voids from the μCT for the strut with a diameter of 2 mm and 90° build angle. Table 4 showed the characterization of internal voids. The average void size was in the order of 30 μm which was comparable to the powder's size. In addition, the void effective diameters in struts with 45° build angle were generally smaller than those with 90° build angle. Nonetheless, it was worth noting that the build direction relative to CT scanning could affect the difference of the void sizes in the 90° and 45° specimens. For example, flat defects such as those from the lack of fusion could be harder to identify with the CT in certain orientations.

Table 4 summarized the volume fraction of internal voids for all SS samples. The overall volume fraction was less than 1% for all samples. The SS samples with 45° build angle provided a smaller volume fraction of voids than those with 90° build angle. A similar observation was reported by Awd et al. [43] and Murchio et al. [41]. One possible reason could come from the larger melt pool size in samples with 45° build angle as previously mentioned. In addition, according to Fig. 2a, it was noticed that struts were placed onto the solid substrate by the order of their size. Thus, struts, which were placed in the middle, had a higher possibility to be affected by spattering from neighboring struts. Therefore, it was seen in Table 4 that struts with diameters of 0.75 and 1 mm, which were placed in the middle, had higher volume fraction of voids than those with diameters of 0.3 and 2 mm, which were located at the edges of the build substrate. In addition to the mentioned reason, the sample location on the build plate and their relative direction with the gas flow may also have an impact on internal porosities [44,45].

The CAD and CAD with voids models were constructed to compare the effect of internal voids on mechanical responses. The inclusion of voids in the CAD model could be seen in Fig. 5c. The mesh sensitivity analysis of internal voids was performed and included in the appendix. According to the sensitivity results, the mesh size around voids was approximately one-fifth of a void diameter. Fig. 10 showed the numerical results for a strut with voids. An image was collected at the strut's total strain of approximately 1%. The equivalent plastic strain was shown for both outer surfaces and internal voids. It was seen that while the development of plastic strain was yet observed at the outer surface, the plastic strain started to form around the voids due to the stress concentra-

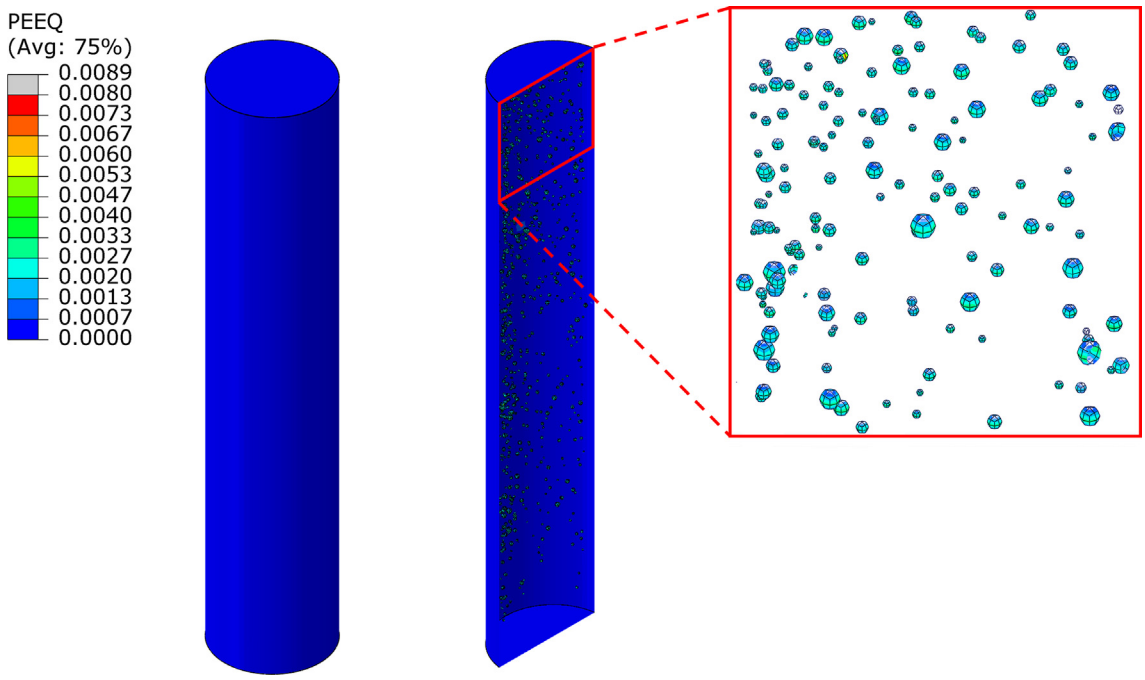

Fig. 10. Predicted equivalent plastic strain (PEEQ) for the SS model with the diameter of 2 mm and internal voids.

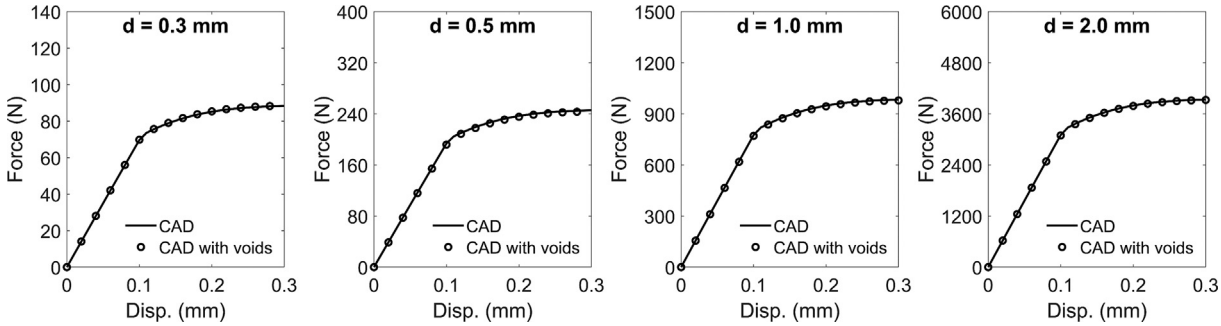

Fig. 11. Predicted Force-Displacement behaviors for CAD and CAD with voids models of SS samples with 90° of build angle.

tion. Therefore, it was expected that the presence of internal voids could have an impact on mechanical responses. Surprisingly, Fig. 11 showed the prediction of Force-Displacement behaviors for CAD and CAD with voids models. Results indicated that there was a negligible difference between mechanical responses for both models. This observation implied that even though the presence of voids may affect the plastic strain localization, they had a little influence on elastic and initial yielding responses, in contrast with external defects described in Section 4.2 which were found to have a more pronounced impact on both values. This remark agreed well with a previous study by Voisin et al. [46] who experimentally studied the influence of the sample size and build orientation on the mechanical response of the L-PBF of Ti-6Al-4V. They reported that the presence of voids at low volume fraction (<1%) mostly governs the failure behaviors, but not yielding and uniform elongation.

Furthermore, while a spherical void was considered in the current study, non-spherical voids may have a greater impact on damage behaviors. The effect of void shapes on plastic damage behaviors was studied numerically by Liu et al. [47]. Both the void aspect ratio and its orientation relative to the loading direction were found to be comparably important. According to Liu et al. [47], the yielding behaviors of spherical and non-spherical voids differed by about 5%.

4.4. Influence of local properties and the effect of μCT voxel sizes

The competition between defects, residual stress, and microstructures on mechanical response are complicated [48]. In previous sections, we evaluated the effect of internal and external defects. Nonetheless, other factors such as residual stress and microstructural features could also play a very important role in mechanical behaviors. Therefore, the ST samples, as described in Fig. 2, were subjected to the mechanical test. The mean diameters shown Table 5 were used for stress calculation.

Fig. 12 illustrated experimental results for stress–strain behaviors of the ST samples. A minimum number of three tests were performed for each condition. Reasonable repeatability in experimental results was seen for all samples. According to Fig. 12, size's dependent behaviors were greatly discernible. The strain at failure reduced significantly with sample' size. And the samples with 90° build angle had the greater failure strain than those with 45° build angle. These results correlated well with external defects found in the SS samples, which tended to be more severe for small samples, especially those with 45° build angle.

In addition to the strain at failure, the yield strength also showed a strong dependency on the sample size and build orientation. According to experimental results shown in Fig. 12, the Voce

Table 5
Mean and standard deviation of the equivalent diameter of the ST samples characterized from the μCT images.

d (mm)	90°		45°	
	μ_d (mm)	s_d (mm)	μ_d (mm)	s_d (mm)
0.3	0.339	0.003	0.378	0.007
0.5	0.512	0.005	0.523	0.007
1	0.928	0.005	0.953	0.008
2	1.911	0.004	1.896	0.006

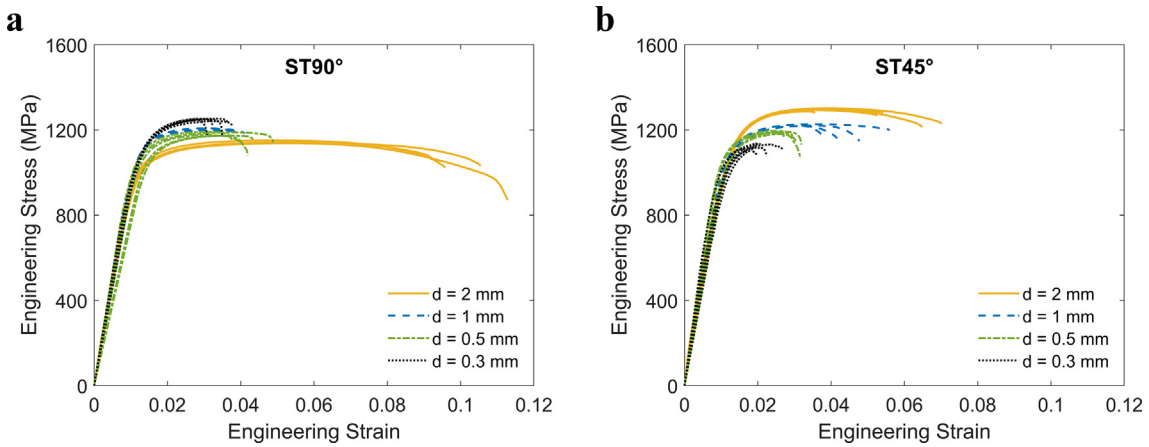

Fig. 12. Experimental results of stress–strain responses for ST samples with a) 90° build angle and b) 45° build angle.

Table 6
Constants for Voce plasticity models, Eq. (1), fitted from experimental results shown in Fig. 12.

d (mm)	90°			45°		
	σ_{y0} (MPa)	H (MPa)	β	σ_{y0} (MPa)	H (MPa)	β
0.3	1107	185.9	188.7	1042	122.1	268.3
0.5	1084	139	172.4	1092	133	224.2
1	1097	140.3	207.1	1067	196.4	184.9
2	1015	177	117	1113	226.9	179.4

material model as shown in Eq. (1) was used to fit with experimental flow stress. The Voce material constants (σ_{y0}, H, and β) for different samples were fitted and shown in Table 6. According to the initial yield strength (σ_{y0}) reported in Table 6, it was seen that the initial yield strength increased when the diameters were reduced for samples with 90° build angle. Similar behavior was observed experimentally by Barba et al. [28]. They showed that small samples would exhibit smaller grain morphologies due to the rapid cooling behaviors. Subsequently, smaller grains led to an increase in the yield strength because of the grain boundary strengthening. The rationale was supported by another experiment by Razavi et al. [49] who studied the effect of build thickness on properties of Ti-6Al-4V from Electron Beam Melting.

However, the reverse trend of σ_{y0} was seen for samples with 45° build angle, where the yield strength was higher with larger samples. Possible explanations could be from different thermal histories, residual stress profiles owing to different orientations, or sample's deflection due to stress relaxation (image shown in the appendix). However, a high-fidelity thermomechanical simulation would be needed to estimate the magnitude of such effects [32,50]. Of note, even though the size- and orientation-dependent properties were noticeable in as-built conditions, they may be alleviated through the heat treatment as shown by Weißmann et al. [51]. However, it was the primary purpose of the present work to evaluate possible numerical discrepancies competed between geometrical defects and varied as-built properties.

Thus, we simulated the ST specimens with diameters of 0.3 and 2 mm. Not only were CAD and μCT models compared, but also the uncertainty from varied local properties. Based on the Voce material models shown in Table 6, the properties of struts with diameters of 0.3 and 2 mm were utilized to represent the upper and lower bounds of the property variation. It was obvious that μCT models with suitable properties of respective sizes would show the closest agreement with experimental results. Therefore, they could be considered as the benchmarking models. Fig. 13 showed numerical results for the ST specimens of both diameters. According to Fig. 13, the discrepancies from benchmarking results were seen when CAD geometries and inappropriate material properties were utilized. Nonetheless, it was important to evaluate the contribution of each factor.

Therefore, Fig. 14 compared the maximum force between experiments and numerical simulations of several variants. The right-side of Fig. 14 was from μCT model, implying that only the effect of varied properties was considered. On the other hand, the left-side of Fig. 14 was from CAD model, meaning that numerical errors could come from both geometries and varied properties. Based on Fig. 14, geometrical errors and varied properties could contribute to numerical discrepancies of 21 and 11 % for the strut

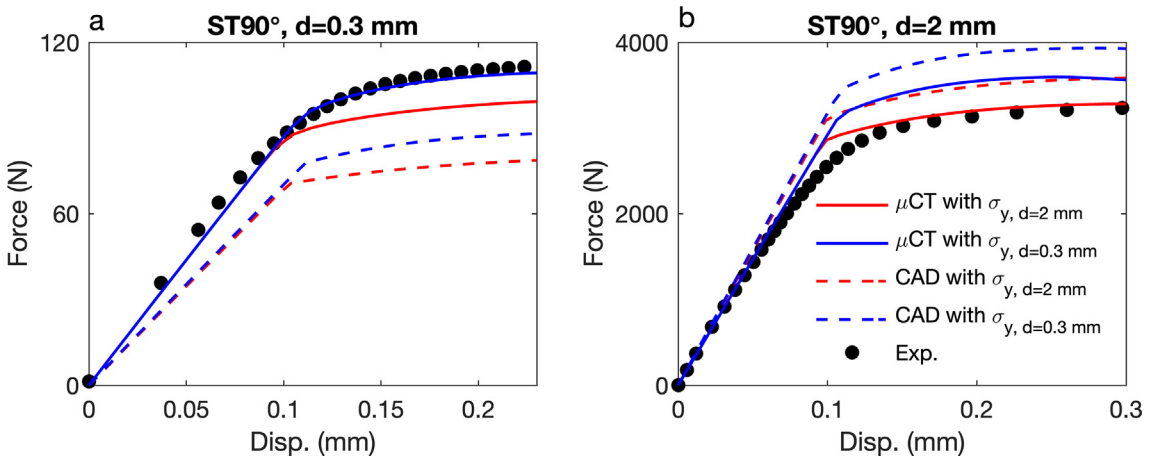

Fig. 13. Comparison between experimental results and the numerical simulation with inclusion of geometrical defects and varied properties for the ST specimens of 90° build angle with diameters of 0.3 and 2 mm (a,b).

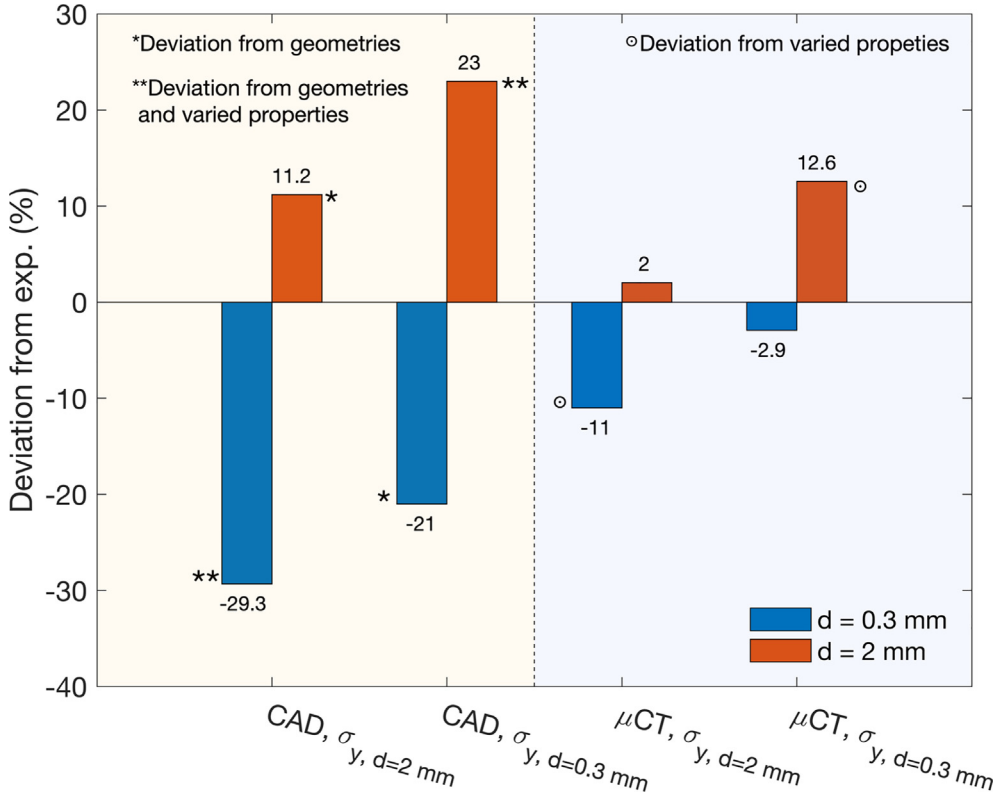

Fig. 14. Force deviation between experiments and numerical simulations of the ST specimens with 90° build angle and with the inclusion of geometrical defects and varied properties.

of 0.3 mm diameter, respectively. Nevertheless, the contribution from both factors became 11.2 and 12.6 % for the strut of 2 mm diameter. It was seen that both geometrical errors and varied properties were not negligible for both strut sizes even though the former was more dominant in a small strut. Therefore, it is critical for these effects to be accounted in the design of AM lattice structures.

In addition to geometrical errors and varied properties, the μCT voxel size could be another sensitivity that may affect the mechanical prediction due to different resolutions of detected surface profiles. Therefore, we performed the numerical simulation of both SS and ST specimens with a diameter of 0.3 mm. Both samples were scanned with voxel sizes of 7 and 12 μm, respectively. The same material models and mesh size were also utilized so that only the sensitivity from surface profiles was revealed. Based on Fig. 15A, the sample with a smaller voxel size exhibited clearly a more distinctive roughness profile. Accordingly, even though the plastic localization was seen for both samples, more localization sites were observed for the model with a smaller voxel size as seen from Fig. 15B. For a global response as shown in Fig. 15C, the difference in the predicted forces was approximately around 5%. Thus, it was seen that the resolution of μCT affected both global and local responses. Therefore, sensitivity from the μCT resolution should be taken into consideration.

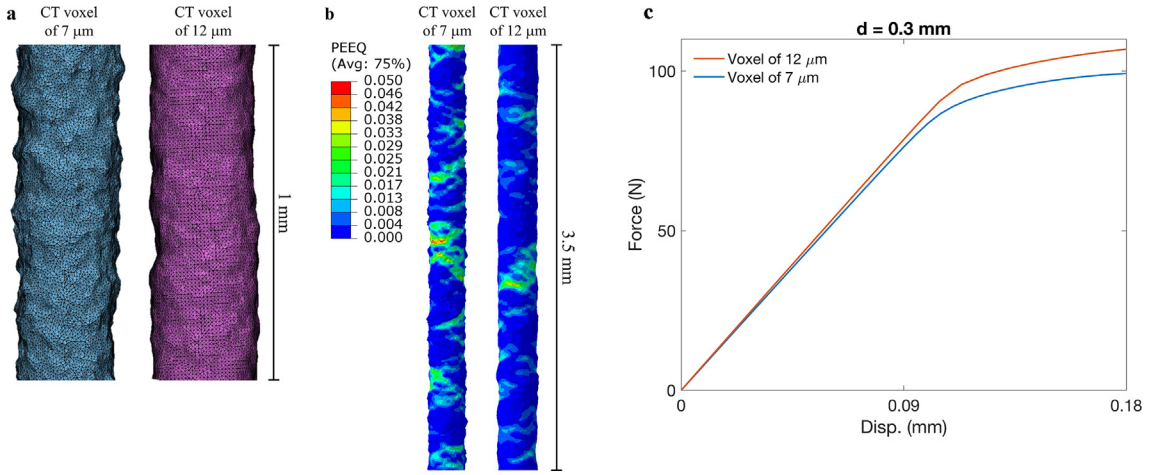

Fig. 15. a) Mesh and surface profiles for the strut of 0.3 mm scanned under the μCT voxel size of 7 and 12 μm, b) the contour of the equivalent plastic strain (PEEQ), and c) Predicted Force-Displacement behaviors.

4.5. Perspectives

As seen from both experimental and numerical analyses, many factors significantly affected mechanical behaviors. Sizing inaccuracy, local surface defects, microstructures, and residual stress could play equally important roles in controlling mechanical responses. Predicted mechanical behaviors using bulk properties and as-designed models could diverge from test results by up to 30%. Followings are our perspectives to alleviate and obtain a more thorough understanding of these issues.

- Concerning the elastic and yielding behaviors, sizing inaccuracy is arguably among the most important geometrical factors. It can vary depending on shapes and process conditions. While using the μCT can provide comprehensive evaluation [26], it is highly resource-consuming and may not be suitable for expandable sample spaces. Several machine learning approaches could assist in this regard [52]. In addition, replacing hatching scan strategies with a single point exposure may simplify the complexity in the build process, thus, allow the improvement of the geometrical accuracy [53].
- Thermomechanical models have been used to reveal the evolution of temperature, microstructure, and residual stress formation in bulk samples [54,55]. Nonetheless, in our opinion, they were rarely used to evaluate size-dependent behaviors. The extension of these models would be beneficial for the assessment of the impact of residual stress and size-dependent microstructures.
- Surface defects would be among the controlling factors of damage behaviors [27]. Nonetheless, we showed that the CT voxel size can significantly affect the evaluation of surface defects. Since the resolution of CT is limited by sample size, we suggest the database of defects build-up from a single strut and utilize that to reconstruct more complex lattice models. Lozanovski et al. [25] successfully demonstrated this notion. However, the inclusion of damage models was yet performed and could be an interesting topic for a future study.

5. Conclusion

The present study investigated the manufacturing defects which could affect the mechanical responses of additively manufactured lattice struts. There were five different defects of interest including undersizing/oversizing, diameter variation, offset of the cross section, internal voids, and local mechanical properties. Samples were made with different diameters from 0.3 to 2 mm and build orientations of 45° and 90°. The primary aim was to quantify different size- and orientation-dependent defects and to reveal the synergetic effect of each defect on the elastic and initial yielding behaviors. Both non-destructive and destructive experiments, and numerical simulations were carried out. Several variations of numerical models were studied, namely, the CAD model referring to strut models with as-designed diameters, the μCT model which directly converted the model from μCT to the FE model, and the Avg model which accounted for the mean equivalent diameter from the μCT. In addition, the CAD model with voids was also created using the effective diameter from the μCT to examine the influence of internal defects. The conclusion could be found as follows.

1. Additively manufactured lattice struts could exhibit both undersizing and oversizing, where the maximum variances was about 15% for samples explored in the present study. The diameter variation and the offset of the cross section were more substantial for struts with small diameters, especially with 45° build orientation.
2. For external defects, the undersizing/oversizing, diameter variation, and offset of the cross section played very important roles in the force prediction. The difference in estimated forces between the μCT and CAD models could be as high as 26%. Although the use of the representative Avg model resulted in a remarkable improvement in the FE prediction, the consideration of the local defects was essential for struts with small diameters, especially those with inclined angles.
3. For all the samples explored in the present study, the void volume fraction was less than 1%. Furthermore, numerical results showed that internal voids negligibly affected the elastic and initial yielding even though they could induce localization. Thus, unless the damage prediction was of interest, the inclusion of internal voids could be neglected given the low volume of void fraction.
4. The experimental yield strength varied with the sample size and build orientation. Additionally, the sensitivity analysis showed that both external defects and varied local properties were proportionately important for a large specimen even though the former were more dominant in small samples.
5. The μCT voxel size affected both global mechanical response and localization. More localization sites were seen from a model with smaller voxel size. Therefore, the sensitivity from the voxel size is another factor that is worth considering.

6. Ultimately, the present study investigated and quantified the influence of external and internal defects as well as local properties on mechanical behaviors of additively manufactured lattice struts. These findings could be integrated into the FE model of lattice structures so that they could be developed to provide reasonably accurate mechanical prediction under optimized computational resources.

CRediT authorship contribution statement

Atikom Sombatmai: Methodology, Software, Data curation, Writing - original draft, Visualization, Investigation, Software, Validation, Funding acquisition. **Vitoon Uthaisangsuk:** Writing - review & editing, Investigation, Supervision, Funding acquisition. **Somchai Wongwises:** Writing - review & editing, Supervision, Funding acquisition. **Patcharapit Promoppatum:** Conceptualization, Methodology, Writing - original draft, Writing - review & editing, Investigation, Supervision, Visualization, Validation, Funding acquisition.

Declaration of Competing Interest

The authors declare that they have no known competing financial interests or personal relationships that could have appeared to influence the work reported in this paper.

Acknowledgement

The research was supported by Research Strengthening Project of the Faculty of Engineering, King Mongkut's University of Technology Thonburi, the Coordinating Center for Thai Government Science and Technology Scholarship Students (CSTS) and National Science and Technology Development Agency (NSTDA). The third author acknowledges the support provided by the "Research Chair Grant" National Science and Technology Development Agency (NSTDA). Authors are thankful for Kitti Sirimongkolniwat from TRUMPF Ltd. and Dr. Keita Ono from Mahidol University for their helps with sample fabrication.

Data availability

The raw/processed data required to reproduce these findings cannot be shared at this time as the data also forms part of an ongoing study.

References

[1] M. Attaran, The rise of 3-D printing: the advantages of additive manufacturing over traditional manufacturing, Bus. Horiz. 60 (5) (2017) 677–688, https://doi.org/10.1016/j.bushor.2017.05.011.
[2] A. Gisario, M. Kazarian, F. Martina, M. Mehrpouya, Metal additive manufacturing in the commercial aviation industry: a review, J. Manuf. Syst. 53 (2019) 124–149, https://doi.org/10.1016/j.jmsy.2019.08.005.
[3] X. Zheng, H. Lee, T.H. Weisgraber, M. Shusteff, J. DeOtte, E.B. Duoss, J.D. Kuntz, M.M. Biener, Q. Ge, J.A. Jackson, S.O. Kucheyev, N.X. Fang, C.M. Spadaccini, Ultralight, ultrastiff mechanical metamaterials, Science 344 (6190) (2014) 1373–1377, https://doi.org/10.1126/science:1252291.
[4] T. Maconachie, M. Leary, B. Lozanovski, X. Zhang, M. Qian, O. Faruque, M. Brandt, SLM lattice structures: properties, performance, applications and challenges, Mater. Des. 183 (2019) 108137, https://doi.org/10.1016/j.matdes.2019.108137.
[5] F. Zhu, G. Lu, D. Ruan, Z. Wang, Plastic deformation, failure and energy absorption of sandwich structures with metallic cellular cores, Int. J. Protect. Struct. 1 (4) (2010) 507–541, https://doi.org/10.1260/2041-4196.1.4.507.
[6] M. Mohsenizadeh, F. Gasbarri, M. Munther, A. Beheshti, K. Davami, Additively-manufactured lightweight Metamaterials for energy absorption, Mater. Des. 139 (2018) 521–530, https://doi.org/10.1016/j.matdes.2017.11.037.
[7] V.V. Vasiliev, V.A. Barynin, A.F. Razin, Anisogrid composite lattice structures – Development and aerospace applications, Compos. Struct. 94 (3) (2012) 1117–1127, https://doi.org/10.1016/j.compstruct.2011.10.023.
[8] W. Tao, M.C. Leu, Design of lattice structure for additive manufacturing, in: 2016 International Symposium on Flexible Automation (ISFA), IEEE, Cleveland, OH, USA, 2016, pp. 325–332, https://doi.org/10.1109/ISFA.2016.7790182.
[9] S. Arabnejad, B. Johnston, M. Tanzer, D. Pasini, Fully porous 3D printed titanium femoral stem to reduce stress-shielding following total hip arthroplasty: FULLY POROUS 3D PRINTED TITANIUM FEMORAL STEM, J. Orthop. Res. 35 (8) (2017) 1774–1783, https://doi.org/10.1002/jor.v35.810.1002/jor.23445.
[10] M. Smith, Z. Guan, W.J. Cantwell, Finite element modelling of the compressive response of lattice structures manufactured using the selective laser melting technique, Int. J. Mech. Sci. 67 (2013) 28–41, https://doi.org/10.1016/j.ijmecsci.2012.12.004.
[11] L. Liu, P. Kamm, F. García-Moreno, J. Banhart, D. Pasini, Elastic and failure response of imperfect three-dimensional metallic lattices: the role of geometric defects induced by Selective Laser Melting, J. Mech. Phys. Solids 107 (2017) 160–184, https://doi.org/10.1016/j.jmps.2017.07.003.
[12] A.R. Nassar, M.A. Gundermann, E.W. Reutzel, P. Guerrier, M.H. Krane, M.J. Weldon, Formation processes for large ejecta and interactions with melt pool formation in powder bed fusion additive manufacturing, Sci. Rep. 9 (2019) 1–11.
[13] P. Promoppatum, S.-C. Yao, Analytical evaluation of defect generation for selective laser melting of metals, Int. J. Adv. Manuf. Technol. 103 (1-4) (2019) 1185–1198.
[14] P. Promoppatum, R. Onler, S.-C. Yao, Numerical and experimental investigations of micro and macro characteristics of direct metal laser sintered Ti-6Al-4V products, J. Mater. Process. Technol. 240 (2017) 262–273.
[15] S. Liu, Y.C. Shin, Additive manufacturing of Ti6Al4V alloy: a review, Mater. Des. 164 (2019) 107552, https://doi.org/10.1016/j.matdes.2018.107552.
[16] A. Du Plessis, I. Yadroitsev, I. Yadroitsava, S.G. Le Roux, X-ray microcomputed tomography in additive manufacturing: a review of the current technology and applications, 3D Print. Addit. Manuf. 5 (2018) 227–247.
[17] M. Leary, M. Mazur, J. Elambasseril, M. McMillan, T. Chirent, Y. Sun, M. Qian, M. Easton, M. Brandt, Selective laser melting (SLM) of AlSi12Mg lattice structures, Mater. Des. 98 (2016) 344–357, https://doi.org/10.1016/j.matdes.2016.02.127.
[18] M. Leary, M. Mazur, H. Williams, E. Yang, A. Alghamdi, B. Lozanovski, X. Zhang, D. Shidid, L. Farahbod-Sternahl, G. Witt, I. Kelbassa, P. Choong, M. Qian, M. Brandt, Inconel 625 lattice structures manufactured by selective laser melting (SLM): mechanical properties, deformation and failure modes, Mater. Des. 157 (2018) 179–199, https://doi.org/10.1016/j.matdes.2018.06.010.
[19] L. Boniotti, S. Beretta, S. Foletti, L. Patriarca, Strain concentrations in BCC micro lattices obtained by AM, Procedia Struct. Integr. 7 (2017) 166–173, https://doi.org/10.1016/j.prostr.2017.11.074.
[20] L. Geng, W. Wu, L. Sun, D. Fang, Damage characterizations and simulation of selective laser melting fabricated 3D re-entrant lattices based on in-situ CT testing and geometric reconstruction, Int. J. Mech. Sci. 157–158 (2019) 231–242, https://doi.org/10.1016/j.ijmecsci.2019.04.054.
[21] M.R. Karamooz Ravari, M. Kadkhodaei, M. Badrossamay, R. Rezaei, Numerical investigation on mechanical properties of cellular lattice structures fabricated by fused deposition modeling, Int. J. Mech. Sci. 88 (2014) 154–161, https://doi.org/10.1016/j.ijmecsci.2014.08.009.
[22] H. Lei, C. Li, J. Meng, H. Zhou, Y. Liu, X. Zhang, P. Wang, D. Fang, Evaluation of compressive properties of SLM-fabricated multi-layer lattice structures by experimental test and μ-CT-based finite element analysis, Mater. Des. 169 (2019) 107685, https://doi.org/10.1016/j.matdes.2019.107685.
[23] M.R.K. Ravari, S.N. Esfahani, M.T. Andani, M. Kadkhodaei, A. Ghaei, H. Karaca, M. Elahinia, On the effects of geometry, defects, and material asymmetry on the mechanical response of shape memory alloy cellular lattice structures, Smart Mater. Struct. 25 (2) (2016) 025008, https://doi.org/10.1088/0964-1726/25/2/025008.
[24] M. Dallago, B. Winiarski, F. Zanini, S. Carmignato, M. Benedetti, On the effect of geometrical imperfections and defects on the fatigue strength of cellular lattice structures additively manufactured via Selective Laser Melting, Int. J. Fatigue 124 (2019) 348–360, https://doi.org/10.1016/j.ijfatigue.2019.03.019.
[25] B. Lozanovski, M. Leary, P. Tran, D. Shidid, M. Qian, P. Choong, M. Brandt, Computational modelling of strut defects in SLM manufactured lattice structures, Mater. Des. 171 (2019) 107671, https://doi.org/10.1016/j.matdes.2019.107671.
[26] X.Z. Zhang, H.P. Tang, M. Leary, T. Song, L. Jia, M. Qian, Toward manufacturing quality Ti-6Al-4V lattice struts by selective electron beam melting (SEBM) for lattice design, Jom 70 (9) (2018) 1870–1876.
[27] J. Pegues, M. Roach, R. Scott Williamson, N. Shamsaei, Surface roughness effects on the fatigue strength of additively manufactured Ti-6Al-4V, Int. J. Fatigue 116 (2018) 543–552.
[28] D. Barba, C. Alabort, Y.T. Tang, M.J. Viscasillas, R.C. Reed, E. Alabort, On the size and orientation effect in additive manufactured Ti-6Al-4V, Mater. Des. 186 (2020) 108235, https://doi.org/10.1016/j.matdes.2019.108235.
[29] C. Phutela, N.T. Aboulkhair, C.J. Tuck, I. Ashcroft, The effects of feature sizes in selectively laser melted Ti-6Al-4V parts on the validity of optimised process parameters, Materials 13 (1) (2020) 117, https://doi.org/10.3390/ma13010117.
[30] Z. Dong, X. Zhang, W. Shi, H. Zhou, H. Lei, J. Liang, Study of size effect on microstructure and mechanical properties of AlSi10Mg samples made by selective laser melting, Materials 11 (12) (2018) 2463, https://doi.org/10.3390/ma11122463.
[31] M. Benedetti, A. du Plessis, R.O. Ritchie, M. Dallago, S.M.J. Razavi, F. Berto, Architected cellular materials: a review on their mechanical properties

towards fatigue-tolerant design and fabrication, Mater. Sci. Eng.: R: Rep. 144 (2021) 100606, https://doi.org/10.1016/j.mser.2021.100606.
[32] P. Promoppatum, V. Uthaisangsuk, Part scale estimation of residual stress development in laser powder bed fusion additive manufacturing of Inconel 718, Finite Elem. Anal. Des. 189 (2021) 103528, https://doi.org/10.1016/j.finel.2021.103528.
[33] P. Promoppatum, S.-C. Yao, Influence of scanning length and energy input on residual stress reduction in metal additive manufacturing: numerical and experimental studies, J. Manuf. Processes 49 (2020) 247–259.
[34] P. Promoppatum, S.-C. Yao, P.C. Pistorius, A.D. Rollett, A comprehensive comparison of the analytical and numerical prediction of the thermal history and solidification microstructure of inconel 718 products made by laser powder-bed fusion, Engineering 3 (5) (2017) 685–694, https://doi.org/10.1016/J.ENG.2017.05.023.
[35] E28 Committee, Test Methods for Tension Testing of Metallic Materials, ASTM International, n.d., https://doi.org/10.1520/E0008_E0008M-16AE01.
[36] X. Cao, Y. Jiang, T. Zhao, P. Wang, Y. Wang, Z. Chen, Y. Li, D. Xiao, D. Fang, Compression experiment and numerical evaluation on mechanical responses of the lattice structures with stochastic geometric defects originated from additive-manufacturing, Compos. B Eng. 194 (2020) 108030, https://doi.org/10.1016/j.compositesb:2020.108030.
[37] H. Choo, K.-L. Sham, J. Bohling, A. Ngo, X. Xiao, Y. Ren, P.J. Depond, M.J. Matthews, E. Garlea, Effect of laser power on defect, texture, and microstructure of a laser powder bed fusion processed 316L stainless steel, Mater. Des. 164 (2019) 107534, https://doi.org/10.1016/j.matdes.2018.12.006.
[38] Z. Zhang, D. Jones, S. Yue, P.D. Lee, J.R. Jones, C.J. Sutcliffe, E. Jones, Hierarchical tailoring of strut architecture to control permeability of additive manufactured titanium implants, Mater. Sci. Eng., C 33 (7) (2013) 4055–4062.
[39] B. He, W. Wu, L. Zhang, L. Lu, Q. Yang, Q. Long, K. Chang, Microstructural characteristic and mechanical property of Ti6Al4V alloy fabricated by selective laser melting, Vacuum 150 (2018) 79–83, https://doi.org/10.1016/j.vacuum.2018.01.026.
[40] M. Simonelli, Y.Y. Tse, C. Tuck, Effect of the build orientation on the mechanical properties and fracture modes of SLM Ti–6Al–4V, Mater. Sci. Eng., A 616 (2014) 1–11.
[41] S. Murchio, M. Dallago, F. Zanini, S. Carmignato, G. Zappini, F. Berto, D. Maniglio, M. Benedetti, Additively manufactured Ti–6Al–4V thin struts via laser powder bed fusion: effect of building orientation on geometrical accuracy and mechanical properties, J. Mech. Behav. Biomed. Mater. 119 (2021) 104495, https://doi.org/10.1016/j.jmbbm.2021.104495.
[42] Z. Dong, X. Zhang, W. Shi, H. Zhou, H. Lei, J. Liang, Study of size effect on microstructure and mechanical properties of AlSi10Mg samples made by selective laser melting, Materials 11 (2018) 2463, https://doi.org/10.3390/ma11122463.
[43] M. Awd, F. Stern, A. Kampmann, D. Kotzem, J. Tenkamp, F. Walther, Microstructural characterization of the anisotropy and cyclic deformation behavior of selective laser melted AlSi10Mg structures, Metals 8 (2018) 825, https://doi.org/10.3390/met8100825.
[44] J. Reijonen, A. Revuelta, T. Riipinen, K. Ruusuvuori, P. Puukko, On the effect of shielding gas flow on porosity and melt pool geometry in laser powder bed fusion additive manufacturing, Addit. Manuf. 32 (2020) 101030, https://doi.org/10.1016/j.addma.2019.101030.
[45] S. Gangireddy, E. Faierson, R. Mishra, Influences of post-processing, location, orientation, and induced porosity on the dynamic compression behavior of Ti–6Al–4V alloy built through additive manufacturing, J. Dyn. Behav. Mater. 4 (2018) 441–451.
[46] T. Voisin, N.P. Calta, S.A. Khairallah, J.-B. Forien, L. Balogh, R.W. Cunningham, A. D. Rollett, Y.M. Wang, Defects-dictated tensile properties of selective laser melted Ti-6Al-4V, Mater. Des. 158 (2018) 113–126, https://doi.org/10.1016/j.matdes.2018.08.004.
[47] L.-Y. Liu, Q.-S. Yang, Y.X. Zhang, Plastic damage of additive manufactured aluminium with void defects, Mech. Res. Commun. 95 (2019) 45–51.
[48] A. Yadollahi, N. Shamsaei, Additive manufacturing of fatigue resistant materials: challenges and opportunities, Int. J. Fatigue 98 (2017) 14–31.
[49] S.M.J. Razavi, B. Van Hooreweder, F. Berto, Effect of build thickness and geometry on quasi-static and fatigue behavior of Ti-6Al-4V produced by Electron Beam Melting, Addit. Manuf. 36 (2020) 101426, https://doi.org/10.1016/j.addma.2020.101426.
[50] P. Promoppatum, A.D. Rollett, Influence of material constitutive models on thermomechanical behaviors in the laser powder bed fusion of Ti-6Al-4V, Addit. Manuf. 37 (2021) 101680, https://doi.org/10.1016/j.addma.2020.101680.
[51] V. Weißmann, P. Drescher, R. Bader, H. Seitz, H. Hansmann, N. Laufer, Comparison of single Ti6Al4V struts made using selective laser melting and electron beam melting subject to part orientation, Metals 7 (3) (2017) 91, https://doi.org/10.3390/met7030091.
[52] H. Hassanin, Y. Alkendi, M. Elsayed, K. Essa, Y. Zweiri, Controlling the properties of additively manufactured cellular structures using machine learning approaches, Adv. Eng. Mater. 22 (3) (2020) 1901338, https://doi.org/10.1002/adem.v22.310.1002/adem.201901338.
[53] E. Onal, A.E. Medvedev, M.A. Leeflang, A. Molotnikov, A.A. Zadpoor, Novel microstructural features of selective laser melted lattice struts fabricated with single point exposure scanning, Addit. Manuf. 29 (2019) 100785, https://doi.org/10.1016/j.addma.2019.100785.
[54] Q. Zhang, J. Xie, Z. Gao, T. London, D. Griffiths, V. Oancea, A metallurgical phase transformation framework applied to SLM additive manufacturing processes, Mater. Des. 166 (2019) 107618, https://doi.org/10.1016/j.matdes.2019.107618.
[55] R.J. Williams, C.M. Davies, P.A. Hooper, A pragmatic part scale model for residual stress and distortion prediction in powder bed fusion, Addit. Manuf. 22 (2018) 416–425.